On the use of CCD area detectors for high-resolution specular X-ray reflectivity

P. Fenter,* J. G. Catalano, C. Park and Z. Zhang

Chemistry Division, Argonne National Laboratory, Argonne, IL 60439, USA. E-mail: fenter@anl.gov

The use and application of charge coupled device (CCD) area detectors for high-resolution specular X-ray reflectivity is discussed. Direct comparison of high-resolution specular X-ray reflectivity data measured with CCD area detectors and traditional X-ray scintillator ('point') detectors demonstrates that the use of CCD detectors leads to a substantial ($\sim$30-fold) reduction in data acquisition rates because of the elimination of the need to scan the sample to distinguish signal from background. The angular resolution with a CCD detector is also improved by a factor of $\sim$3. The ability to probe the large dynamic range inherent to high-resolution X-ray reflectivity data in the specular reflection geometry was demonstrated with measurements of the orthoclase (001)– and α-Al_2O_3 (012)–water interfaces, with measured reflectivity signals varying by a factor of $\sim 10^6$ without the use of any beam attenuators. Statistical errors in the reflectivity signal are also derived and directly compared with the repeatability of the measurements.

1. Introduction

Surface X-ray scattering and reflectivity have been used extensively to probe the structure of both free and buried interfaces (Robinson, 1988, 1991; Feidenhans'l, 1989; Robinson & Tweet, 1992; Als-Nielsen & McMorrow, 2001; Fenter, 2002). The benefits of X-ray scattering as a probe of interfacial structures includes the ability to probe these structures with high resolution, under *in situ* conditions, in real time (*e.g.* during growth or dissolution), as well as the simple and direct relationship between the structure and the measured intensities. One of the primary challenges in performing surface X-ray scattering measurements is the intrinsically weak signal, owing to a combination of the weak interaction strength of X-rays with matter and the small number of atoms participating in a surface diffraction measurement (*e.g.* $\sim$1 monolayer), which necessitates the use of high-brilliance synchrotron X-ray sources. Even when using synchrotron sources the interfacial scattering signal is often substantially smaller than the incoherent background signals (hereafter referred to as background), which are due to both elastic (*e.g.* thermal diffuse scattering) and inelastic (*e.g.* Compton scattering, X-ray fluorescence) processes. Consequently, one of the rate-limiting steps in the acquisition of surface diffraction data is distinguishing signal from background.

Various approaches have been proposed for using area detectors with surface X-ray diffraction measurements to increase the rate of data acquisition. One-dimensional position-sensitive detectors have been used routinely (Robinson *et al.*, 1994). CCD area detectors have been used to image Bragg rods of films at small vertical momentum transfer during film growth, making use of the fact that Bragg rods are tangential to the Ewald sphere for scattering conditions that are largely parallel to the surface plane (Hong *et al.*, 2002). Additionally, CCD area detectors have been widely used to probe diffuse scattering of low-angle surface reflectivity data where specular and diffuse scattering can be probed simultaneously (Naudon & Thiaudiere, 1997). Recently, a pixel array detector for probing surface diffraction data has been described (Schlepütz *et al.*, 2005). In this article we describe the benefits and utility of using a commercially available CCD detector to collect high-resolution specular X-ray reflectivity data, including procedures for data acquisition, reduction and normalization.

2. Background: traditional data acquisition

While the various manifestations of the surface X-ray scattering technique have been well documented (Robinson, 1988, 1991; Feidenhans'l, 1989; Robinson & Tweet, 1992; Als-Nielsen & McMorrow, 2001; Fenter, 2002), the basic outline of a high-resolution X-ray specular reflectivity measurement is described here for completeness. The Ewald sphere construction for a specular X-ray reflectivity measurement is shown schematically in Fig. 1(a). Here, the X-ray beam with wavevector magnitude $|\mathbf{K}| = 2\pi/\lambda$ (X-ray wavelength, λ) is incident on the surface plane at an angle θ, and detected at a scattering angle of 2θ, resulting in a momentum transfer of $\mathbf{Q} = \mathbf{K}_f - \mathbf{K}_i$. We are specifically interested in the case of high-resolution specular reflectivity, which probes the laterally averaged interfacial structure. These measurements typically are performed to <1 Å spatial resolution by measuring the structure factor well into the regime where the tails of the substrate Bragg peaks modulate the interfacial reflectivity,
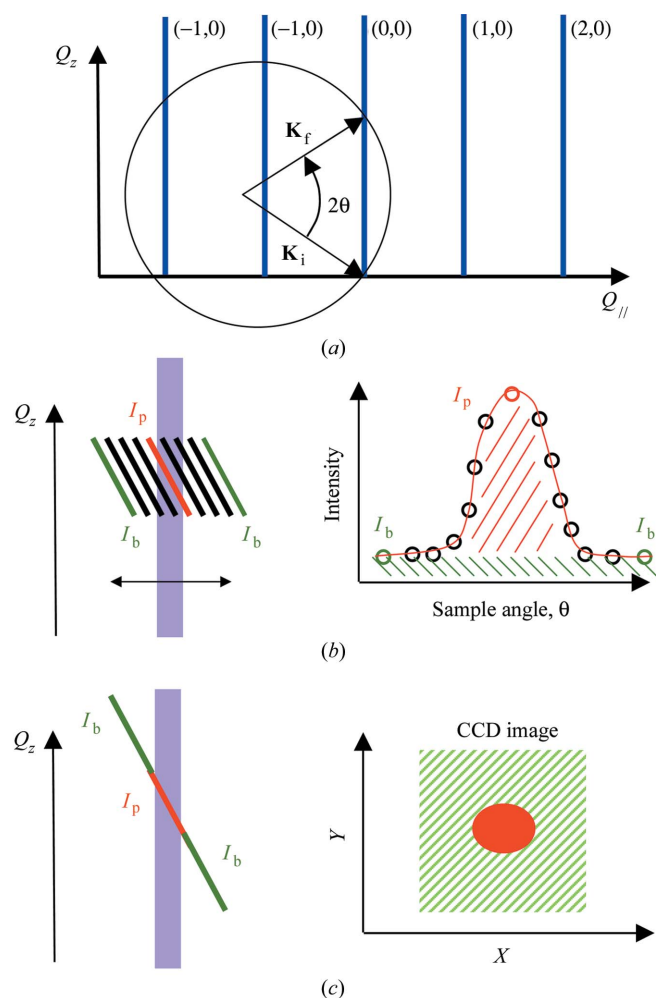
Figure 1
(a) Ewald sphere construction of surface reciprocal space, including both specular and non-specular rods, showing the incident and reflected X-ray beam, the momentum transfer $\mathbf{Q} = \mathbf{K}_f - \mathbf{K}_i$ and the scattering angle 2θ. (b) Schematic of a rocking scan in which the sample angle is rotated as the detector is held fixed. This effectively scans the detector resolution function across the crystal truncation rod resulting in a peak super-imposed on flat background. (c) Schematic of the use of a CCD detector to image the reflected X-ray beam, in which the specularly reflected beam appears as a spot (red region) on a flat background count rate (green hatched region) with the sample and detector held fixed.

often referred to as crystal truncation rod (CTR) profiles (Robinson, 1986).

For the case of specular reflectivity described here, $\mathbf{Q} = Q_z = (2\pi/d_{001})L$, where d_{001} is the Bragg plane spacing and L is in reciprocal lattice units (r.l.u.). The range of angles within the scattering plane accepted by the finite detector slit size (i.e. the resolution function) is characterized by an angular width $\Delta(2\theta) \simeq d/R$, where d is the detector slit size and R is the sample–detector distance. The scattering signal is obtained from the overlap of the resolution function when it is super-imposed on the specular rod, shown schematically in Fig. 1(b). Separating signal from background is normally done by scanning the sample angle θ, resulting in a 'rocking scan' where the sample angle is scanned through the specular reflection condition and in which the signal appears as a peak superimposed on a flat or linearly varying background

(Fig. 1b). The background is observed when the sample angle is sufficiently far from the specular condition (shown as the green detector resolution functions in Fig. 1b), when the interfacial reflectivity is blocked by the detector slits. The quantity of interest in a surface-scattering measurement is normally the 'integrated intensity', which for a rocking scan is the area under the peak after the background is subtracted, shown schematically as the red hatched region in Fig. 1(b). In the case where the lateral width of the specular rod, $\Delta Q_{//}$, is narrower than the projected lateral size of the resolution function, $K\Delta(2\theta)\sin(\theta)$, the background-subtracted peak height, $I_p - I_b$, is independent of the detector slit size; the peak width is $\Delta\theta = \Delta(2\theta)/2$, leading to an integrated intensity of $\sim (I_p - I_b)\Delta\theta = (I_p - I_b)\Delta(2\theta)/2$. This integrated intensity is proportional to the detector slit size, $\Delta(2\theta)$, since that determines the length of the specular rod that is integrated, corresponding to vertical resolution in reciprocal space of $\Delta Q_z = K\Delta(2\theta)\cos(\theta)$. The use of rocking scans, while not strictly necessary, is extremely useful for obtaining precise structure factors over the large range of incident angles, e.g. to avoid systematic errors due to changes in the width of the rocking curve as a function of Q due to step structures (Fenter et al., 2001).

While this procedure results in precisely measured structure factors, a rocking scan must be performed at each momentum transfer. Data acquisition is often slow, especially when the signal level is small or the background level is high, with typically 30–50 points in a rocking scan. Integration times of 1–2 min per point are not uncommon when the reflectivity is weak, in which case a structure factor at a single Q may require 1–2 h of data acquisition time, and a complete reflectivity measurement may require ~6–24 h. Distinguishing the signal from background is therefore an important rate-limiting step in data acquisition.

3. High-resolution X-ray reflectivity measurements with a CCD detector

There are two fundamental differences in using a CCD detector with respect to that of a point detector. The first obvious difference is that an area detector spatially resolves the scattered radiation into the individual pixels. Since the signal and backgrounds have different angular dependencies, this has benefits in terms of the rate of data acquisition, monitoring sample alignment and understanding the source of extraneous signals. The second difference is that the CCD detector integrates in time and therefore does not count individual photons as is done with a scintillator detector (e.g. using pulse-height analysis). Consequently, while a CCD is insensitive to count rate, it is limited by the pixel well depth. The conversion of CCD counts to X-ray photons must also be done in order to estimate the errors due to counting statistics. The CCD also has essentially no energy resolution and therefore care must be taken to ensure that the measured signals do not correspond to extraneous sources (e.g. harmonics of the incident-beam energy, sample fluorescence). The relative benefits of reduction of counting time with the

possible costs of the loss of pulse-counting capability are addressed below

3.1. Data collection

Substantial time savings can be obtained, in principle, with the use of area detectors (Fig. 1c). By substituting an area detector for a normal scintillator ('point') detector, the signal and background can be distinguished with a fixed sample orientation. The scattered signal is spatially resolved as a spot (due to intersection of the specular rod with the Ewald sphere) superimposed on a flat or linearly varying incoherent background. Since the signal and background are measured simultaneously, one can expect that data acquisition will be 30–50 times faster than in traditional measurements where the sample must be scanned. This is conceptually similar to a procedure described previously in which interfacial reflectivity was probed using an open-slit configuration so that the measured intensity is due solely to the overlap of the crystal truncation rod with the Ewald sphere without the need for a rocking scan (Specht & Walker, 1993). Some of the challenges of using a CCD detector include measuring reflectivity signals that vary by factors of $>10^6$ while simultaneously requiring that the signals be measured with high precision and accuracy (ideally within $\sim1\%$ of the true value). In many cases the signal can be substantially weaker than the incoherent background inherent to these measurements. It is also necessary that the uncertainty in the scattered signal be quantified so that the data can be quantitatively analyzed through various schemes [e.g. traditional least-squares minimization (Robinson, 1988, 1991; Feidenhans'l, 1989; Robinson & Tweet, 1992; Als-Nielsen & McMorrow, 2001; Fenter, 2002) or direct inversion (Fenter & Zhang, 2005; Lyman et al., 2005; Robinson et al., 2005)].

The typical experimental set-up with the CCD detector is shown in Fig. 2, at the 11-ID-D endstation at the BESSRC/XOR sector of the Advanced Photon Source (Beno, Engbretson et al., 2001; Beno, Jennings et al., 2001). A small-format Roper scientific (PI-SCX) X-ray CCD detector (1300 pixels × 1340 pixels, with 0.02 mm pixel size) is mounted on the detector arm of a Psi-C diffractometer. This detector uses a GdOS:Tb phosphor that is coupled to the CCD chip by a 1:1 optical fiber bundle. The diffractometer is controlled with standard commercial software for navigating reciprocal space (i.e. SPEC) based on algorithms described previously for the various diffractometer geometries (Busing & Levy, 1967; Bloch, 1985; Vlieg et al., 1987; You, 1999). After the beam-defining slit, a fast (Uniblitz) X-ray shutter is used to control the X-ray beam exposure to the time when the CCD is acquiring data; a beam flux monitor (e.g. an ion chamber) is used for normalization of data, and a filter box is available to attenuate the beam as needed for strong reflections so that saturation of the CCD detector pixels is avoided. As in the case of traditional data collection, we limit the size of the incident beam so that the beam footprint is well within the boundaries of the sample for all measurements, and consequently no corrections to the data need to be made for beam spill-off.

As is normal for surface-scattering measurements, the experimental set-up makes use of slits on the detector arm to define the range of the Ewald sphere that is probed and to reduce extraneous background signals. During traditional data acquisition with a scintillator detector and rocking scans, a detector slit aperture of ~0.5 mm × 2 mm (within and transverse to the vertical scattering plane, respectively) is typical with a distance between the sample and the detector slits of ~760 mm. When using the CCD detector, the slit must be opened wide enough so that the section of the Ewald
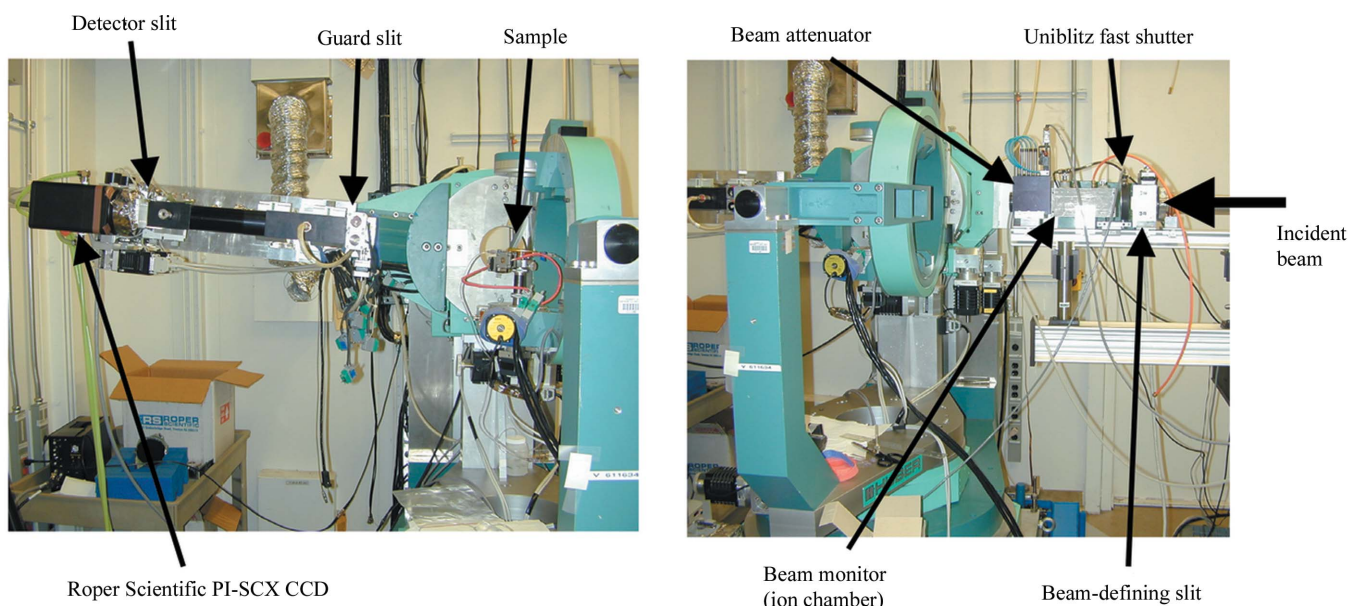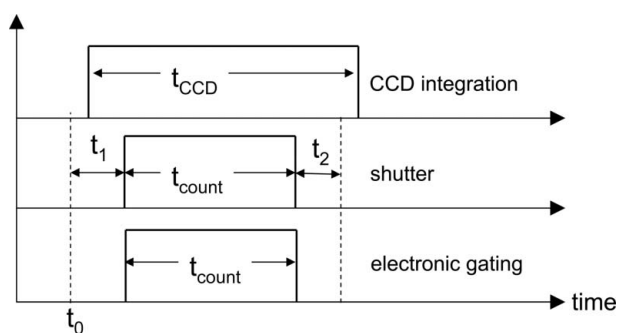

Figure 2
Experimental set-up for the measurements at the BESSRC/XOR beamline 11-ID-D. The incident beam passes through a beam-defining slit, a fast shutter, a beam monitor and a beam attenuator. The reflected beam is detected by the CCD mounted on the detector arm, and the detector solid angle is controlled by the detector slit. Background signals are minimized with a guard slit.

sphere within the detector slits completely spans the specular rod and the background (shown as the green regions in Fig. 1c) is well distinguished from any tails of the specular rod. In this case the scattering intensity is independent of the detector slit size as it is due solely to the overlap of the Ewald sphere with the specular rod. Typical detector slit settings are $\sim$3 mm $\times$ 3 mm. The guard slits are also opened sufficiently wide so that they do not limit the range of reciprocal space that is probed, but are sufficiently small so that they minimize background signals extrinsic to the sample (e.g. from air scatter and beam-defining slits). In this manner we obtain intrinsic background signals that are comparable with those from a high-resolution scattering geometry (normalized to detector solid angle), but with the capability to obtain both signal and background at a given Q with a fixed sample orientation.
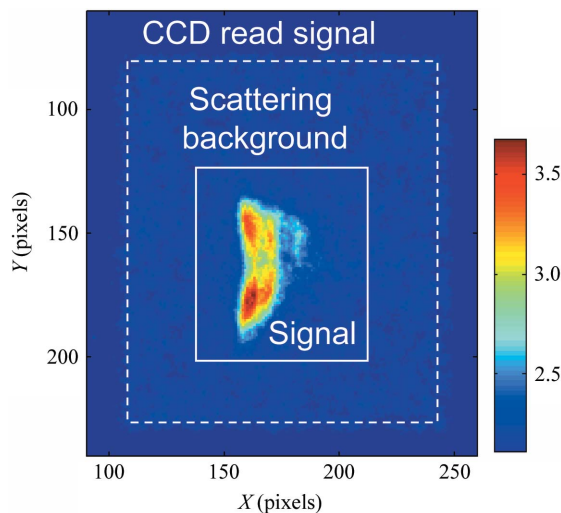
Operational control during measurements is coordinated between a diffractometer computer and a separate dedicated computer that controls the CCD detector. The diffractometer computer is used to navigate reciprocal space and it initiates data acquisition at each selected momentum transfer. A timing diagram for the coordination between these computers is shown schematically in Fig. 3. The diffractometer computer sends a command (at t_0) via an EPICS IOC software interface (Rivers, 2005) through the Ethernet to the CCD computer to initiate the data acquisition for a specified time interval, t_{count}. The CCD camera starts to integrate after a brief delay due to Ethernet communications and the time needed to erase the CCD prior to recording an image. At a later time, t_1, the diffractometer computer simultaneously initiates the opening of the fast shutter and counting of the beam monitor and any other signals, as would otherwise be done with a scintillation detector. The CCD counting time is also extended by a short time, t_2, so that the fast shutter closes before the CCD completes an image ($t_{CCD} = t_1 + t_{count} + t_2$). In this way the scattering signals measured by the CCD and the monitor signals are proportional and the CCD data can be precisely normalized for various counting times necessary to see the full dynamic range of the interfacial reflectivity. We have found that this system routinely works using $t_1 = 0.5$ s and $t_2 = 0.3$ s.

Timing errors (e.g. due to unusual delays in Ethernet communication) are monitored with a DC voltage signal from the CCD controller that is non-zero only during CCD integration, which is converted to pulses using a voltage-to-frequency converter and counted along with the other signals while the electronic gating signal is non-zero (i.e. while the fast shutter is open). Tests of the system for various counting times ranging from 0.1 to 60 s with a surface-reflected beam show no significant changes to the normalized reflectivity due to use of the CCD detector. However, a small loss of monitor signal at short exposure times (<1% loss for 1 s integration, and $\sim$5% loss for 0.2 s integration) was observed due to the use of an ion chamber as a beam flux monitor that is placed after the fast shutter; the finite amplifier integration time leads to a loss of signal that was confirmed separately using a traditional scintillator detector with rocking scans. Such distortions can be avoided by using a monitor based on detection of scattered X-rays using pulse counting with fast electronics.

A typical CCD image of the reflected X-ray beam is shown in Fig. 4. This raw image shows an X-ray beam specularly reflected from an orthoclase–water interface (Fenter et al., 2003) at a reciprocal lattice vector of $L = 1.9$ r.l.u. using a photon energy of 19.5 keV ($d_{001} = 6.48$ Å for orthoclase). This was acquired at the BESSRC/XOR 12-BM beamline. These data (plotted as a two-dimensional image with logarithmic color map) show the specularly reflected X-ray beam superimposed on a large square region corresponding to diffuse 'scattering background' within the $\sim$3 mm $\times$ 3 mm-sized detector slits. Outside of the scattering background region is the CCD read signal and any thermal noise independent of the X-ray beam. The axes of the image (X and Y) correspond in these specular reflectivity measurements to motions along the

Figure 3
Timing diagram for acquisition of data using a CCD detector. The measurement is initiated at t_0, and the CCD detector begins to integrate after a brief delay. At time t_1 the shutter is opened and the electronic gating of the signals is initiated for a specified time period, t_{count}. The CCD integrates for a total time $t_1 + t_{count} + t_2$ to avoid any errors in measured intensity due to timing errors.

Figure 4
The reflected X-ray beam imaged by the CCD detector from an orthoclase (001)–water interface at a specular reflection condition at $L = 1.9$ (r.l.u.), with the logarithmic color scale shown on the right. The solid white line indicates the region that includes the scattering signal, and the dashed white line indicates the defining slit aperture and the corresponding area of the CCD that detects the background signal. Outside of the dashed line, the CCD signal corresponds only to a CCD read signal and any dark counts.
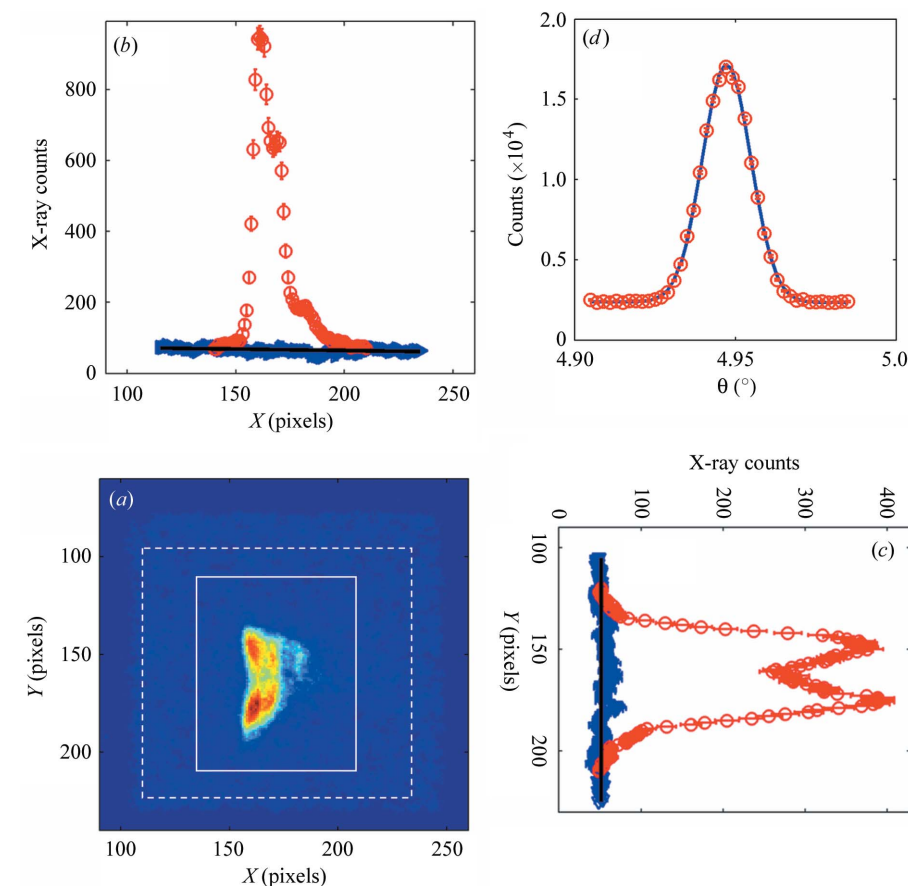
Ewald sphere within and transverse to the vertical scattering plane, respectively. In the present results they correspond to the vertical and horizontal scattering angles, 2θ and ν, that could be used to obtain equivalent trajectories through reciprocal space using a Psi-C diffractometer (You, 1999). The specularly reflected X-ray beam shows a splitting transverse to the scattering plane (along Y) into a doublet associated with the sagittal focusing of the beam. Additional fine structure, primarily within the scattering plane (along X), is associated with a minor mosaic structure of the sample.

3.2. Data conversion and integration

Some care is needed to convert these raw CCD images to structure factors and determine errors associated with photon-counting statistics. In particular, the statistics are limited not by the number of electrons detected at the CCD but by the number of detected X-ray photons. X-ray photons are not counted individually, however, since the CCD detector is an integrating device. This has the advantage that photons are not lost at high count rates due to detector dead-time, and instead are uncounted only if a pixel reaches its maximum capacity.

The electron counts on the CCD must therefore be converted to an equivalent number of X-ray photons, and then counting statistics can be imposed. This is done by subtracting from the CCD image two extrinsic contributions to the image: a 'read signal' which is a fixed offset for all images, and a separate contribution due to detector 'dark counts' that is proportional to the counting time (both subtractions are carried out on a pixel-by-pixel basis). These reference images were obtained by repeated blank images. Calibration of the number of detected electrons per incident X-ray photon is performed by direct comparison to the X-ray scintillator detector. We find an average of ~ 90 electrons are detected for each X-ray photon with an energy of ~ 19.5 keV.
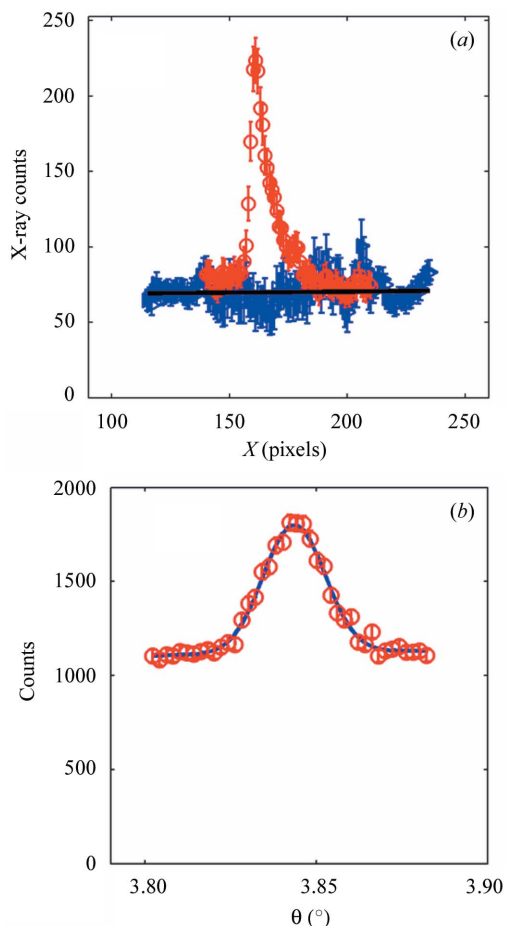
Another subtlety associated with using the CCD detector is that there is some 'blooming' of electrons from a given photon to neighboring pixels. Consequently, raw CCD images may have pixels with a fractional number of detected photons after conversion of electrons counts to photons, especially when the number of detected X-ray photons is small. A simple method to avoid this problem is to use integrated intensities, so that the likelihood of fractional photon counts in a given pixel becomes negligible. Then we can associate the number of electrons detected by the CCD detector (integrated along a line or within an area) with a given number of X-ray photons, and impose uncertainties due to counting statistics on the number of X-ray photons to obtain the associated statistical uncertainty (*i.e.* $\sigma_N = N^{1/2}$, where N is the number of X-ray photons). This is shown in Figs. 5 and 6, in which the effective number of X-ray photons is plotted as one-dimensional integrations of the CCD image along the two axes. In these profiles the signals are integrated along a given direction within the signal box (solid white rectangle in Fig. 5a) resulting in the one-dimensional profile shown as red circles in Figs. 5(b) and 5(c). Similarly, integration of the background signal box exclusive of the signal box (dashed white rectangle in Fig. 5a) results in the one-dimensional background profiles shown as blue triangles in Figs. 5(b) and 5(c). The background level in the one-dimensional profile (and associated uncertainty) is scaled to a level appropriate for comparison with the one-dimensional signal profile since the number of background pixels in the CCD image for a given point in the one-dimensional profile is different from that in the signal box and is not constant across the one-dimensional profiles. Consequently, the one-dimensional profiles show the background signals

Figure 5
Comparison of CCD and scintillator detector measurements of the orthoclase (001)–water interface at specular reflection conditions characterized by $L = 1.90$. (a) Raw CCD image with associated signal and background regions (solid and dashed white boxes, respectively) displayed using a logarithmic color map. Projections of the CCD image are shown along (b) X and (c) Y, where the red symbols indicate the integrated signal region and the blue symbols indicate the background region. (d) Rocking scan of the same sample under identical scattering conditions (except for a smaller detector slit aperture as appropriate for minimizing background with a scintillator detector).

Figure 6
Comparison of CCD and scintillator detector measurements of the orthoclase–water interface at specular reflection conditions characterized by $L = 1.51$, where the surface reflectivity is relatively weak. (a) One-dimensional projection of a CCD image along X. (b) Rocking scans of the same sample under identical scattering conditions (except for a smaller detector slit aperture as appropriate for minimizing background with a scintillator detector).

'under' the signal peak as well as away from the signal (as is normal for rocking-scan analysis). Standard numerical approaches are used to fit the background of the one-dimensional data to a line (Bevington, 1969). The integrated intensity is obtained by numerically subtracting the background (Fenter, 2002). This procedure is carried out separately along the X and Y directions.

A separate method for background subtraction separates the CCD image into two rectangular regions centered on the same point as shown in Fig. 5(a). Under these circumstances the integrated intensity can be obtained analytically as $I = I_{sig} - I_{back}N_{sig}/N_{back}$, where I_{sig} (I_{back}) is the integrated counts in the signal (background) region and N_{sig} (N_{back}) is the number of associated pixels. Photon-counting statistics are then imposed on the integrated X-ray counts in the two regions to estimate the statistical errors. The ultimate derived uncertainty in the signal is obtained by adding in quadrature the semi-quantitative statistical uncertainty for each of the three integrations with the maximum difference between the three integration approaches. This is done because improper

choices of signal or background regions will result in different integrated intensities for these various approaches (and will not be reflected in the derived statistical errors). Consequently any significant discrepancy between these approaches (which is most common when the signal level is small compared with the background signal level) is reflected in the final structure factor as an increased uncertainty due to systematic error.

3.3. Data normalization

Conversion of these integrated intensities to structure factors is obtained with general formalisms developed previously (Robinson, 1988, 1991; Feidenhans'l, 1989; Robinson & Tweet, 1992; Specht & Walker, 1993; Als-Nielsen & McMorrow, 2001; Fenter, 2002). Since the measurement of intensities is different for a rocking scan *versus* the CCD integration, it might be expected that there can be systematic differences in the relationship between structure factors and measured intensities. For measurements with a CCD detector, the sample is fixed. This has the consequence that the degree to which the fixed detector resolution function integrates the truncation rod now depends upon the properties of the incident beam (*e.g.* the angular beam divergence). A general expression for the intensity becomes

$$I(Q_z) = 2(2\pi)^2 I_0 r_o^2 P |F_{HK}(Q_z)|^2 \Delta Q_z(Q_z)/\left[(Q_z A_{uc})^2 \cos(\theta)\right], \quad (1)$$

where I_0 is the incident beam flux (in units of photons s^{-1}), $r_o = 2.818 \times 10^{-5}$ Å is the classical electron radius, P is the polarization factor, F_{HK} is the interfacial structure factor calculated for a single unit cell of the sample for the (H,K) rods with a vertical momentum transfer of Q_z, ΔQ_z is the length of the rod that is integrated in a single image, and A_{uc} is the surface unit-cell area.

If we assume a monochromatic beam with finite beam divergence within the scattering plane, the length of the rod that is integrated depends upon the angular width of the incident beam, $\delta\theta_{beam}$. This results in a detector volume element that is obtained by a transverse displacement of the resolution function of $Q\delta\theta_{beam}$, and the resulting length of the specular rod that is integrated is $\Delta Q_z = 2K \cos(\theta) \delta\theta_{beam}$, as shown in Fig. 7. Consequently the relationship between structure factor and intensity for high-resolution specular reflectivity measurements has the same functional dependence as a function of momentum transfer as that obtained using rocking scans.

3.4. Analysis of CCD images

The one-dimensional projections of the CCD images along either X or Y show the reflected beam superimposed on a flat background within the slit region at both $L = 1.9$ and 1.51 (Figs. 5 and 6). These one-dimensional profiles directly probe the shape of the specular rod convoluted with the incident beam size, and consequently the width of the peak provides a lower limit to the surface domain size, similar to that derived from the width of the rocking scan. In this case the specular rod width in the X projection, $\delta_{2\theta}$, can be used to estimate the
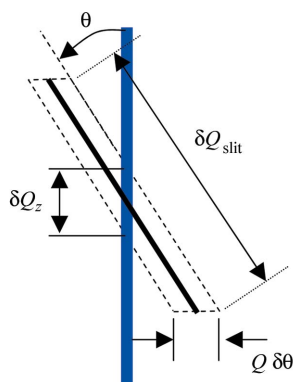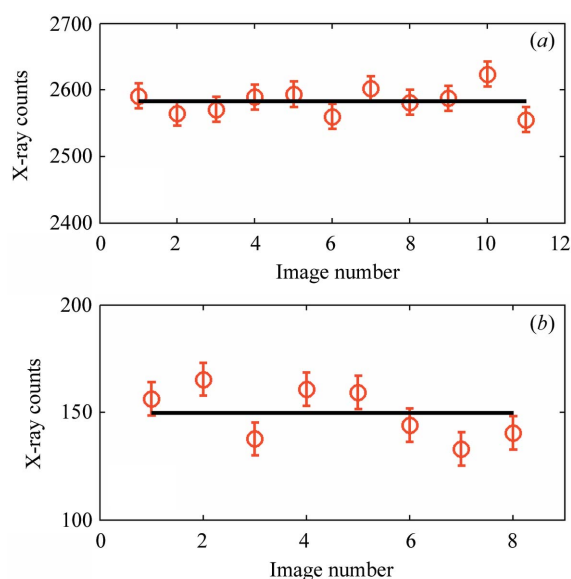
Figure 7
Schematic diagram showing the length of the specular reflectivity rod, δQ_z, integrated in a CCD image, associated with transverse broadening of the detector resolution volume owing to beam divergence, $\delta\theta$.

surface domain size. Here, $\Delta Q_{//} < K\delta_{2\theta}\sin(\theta)$, where $\Delta Q_{//} \simeq 2\pi/D$, and D is the surface domain size. Consequently a lower limit on the surface domain size is $D > 4\pi/[Q_z\delta_{2\theta}]$. For the data at $L = 1.51$ (Fig. 6), we find a peak width of ten pixels (for the sharpest mosaic contribution). At a detector distance of $R = 760$ mm, this corresponds to an angular width $\delta_{2\theta} \simeq 0.015°$ and surface domain sizes of >3.3 µm at $L = 1.51$. The observed peak width can also be compared with the incident-beam size of 0.2 mm which would be expected to give a peak width of about ten pixels on the CCD detector (pixel size of 0.02 mm). Consequently the surface coherence length derived from the image at $L = 1.51$ is largely limited by the incident-beam size and sample mosaic structure. A somewhat smaller lower limit for the domain size, >1.7 µm, is obtained from the data at $L = 1.9$ (Fig. 5), and this appears to be due to a greater mosaic contribution to the line-shape for this particular image.

We can compare these surface domain sizes with that derived from the traditional rocking scan measurements (Figs. 5d and 6b). These data were measured on the same sample under identical conditions as those measured with the CCD detector, except with a scintillator detector using smaller detector slits of 0.5 mm × 2 mm. These traditional measurements reveal a resolution-limited rocking-curve width (i.e. $\Delta\theta = \Delta 2\theta/2$, where $\Delta 2\theta$ is the angular acceptance of the detector slits) with $\Delta\theta = 0.02°$, and derived surface domain sizes of >0.98 µm and >1.2 µm at $L = 1.9$ and 1.51, respectively, which are substantially smaller than the lower limits found with the CCD detector. This is largely due to a better angular resolution when using the CCD detector that can be expected, based on the difference in peak widths, to translate into a ~ 2.7 times better signal-to-background ratio at $L = 1.51$ (the degree of improvement will depend upon details of the experimental geometry including the beam size and detector slit size). The actual signal-to-background ratio is ~ 3.5 times better with the CCD as compared with the scintillator detector at $L = 1.51$. This additional improvement of signal to background with the CCD detector derives from the use of an open transverse detector slit in the traditional measurements. The transverse detector slit size was chosen to be broader than the transverse size of the specular rod during the rocking scan to

insure that the intensity is fully integrated along the direction transverse to the scattering plane (e.g. to avoid errors due to changes in the CTR shape along the rod), thereby increasing the background that is accepted. In contrast, the CCD integration region along the direction transverse to the scattering plane can be optimized during data analysis as the suitability of the integration is then obvious. Since the necessary counting time to distinguish weak signals from a strong background is determined both by the absolute signal size as well as the background signal, this should translate into substantially more precise data or more rapid data acquisition. Consequently the use of a CCD detector provides two substantial benefits for surface diffraction measurements: the ability to acquire data at a fixed sample angle, thereby reducing counting times by factors of 30 to 50, and the better angular resolution afforded by the CCD detector and associated improvements of signal to background.

We have so far assumed that imposing counting statistics on the effective number of detected X-ray photons is appropriate. To demonstrate that this is a reasonable approximation for these data, the variability of repeated measurements at both $L = 1.51$ and $L = 1.9$ are shown in Fig. 8. These plots show the integrated signal (in counts per second) measured with a 10 s integration interval with their derived errors for multiple repeated measurements (note the differences in vertical scale). The horizontal line indicates the average value of each set of measurements. These data show that the variability of the individual data points is consistent with the expected variability due to counting statistics, suggesting that the conversion of CCD counts to detected photons was performed appropriately. Additional measurements show that the derived errors decrease with increasing counting time, as would be expected.

Figure 8
Reproducibility tests for the CCD repeatedly measuring the same scattering condition at (a) $L = 1.9$ and (b) $L = 1.51$. Note the difference in vertical scales for the two sets of data. The black horizontal line indicates the average value for each set of measurements.

We now compare the absolute errors and counting times for the two detector systems for the data shown in Figs. 5 and 6. Using the scintillator detector and the rocking scan, we find a fractional error due to statistics of 0.5% and 5% for the measurements at L = 1.9 and 1.51, respectively, using counting times of 400 s for each complete rocking scan (40 points with 10 s per point). In comparison, the CCD measurement obtained fractional errors of 1% and 8% at L = 1.9 and 1.51, respectively, using counting times of 8 and 20 s, respectively. Consequently the CCD detector obtains comparable statistical error with substantially shorter integration times. Typically, the uncertainties in derived structure factors become dominated by various sources of extrinsic error when specular reflectivity measurements are obtained with excellent statistics. Sources of extrinsic errors include those that are independent of the sample (detector non-linearity, spectrometer alignment) as well as those that depend upon the sample and its environment (surface roughness, water film thickness and interfacial structure) and can be monitored by the evolution of repeated fiducials (*i.e.* repeated measurements taken at fixed scattering conditions throughout a measurement to ensure that the system being studied is stable over the time required to complete an experiment). Fiducials are typically chosen at two scattering conditions that are strongly and weakly sensitive to the surface structure, respectively. Any changes in the experimental system will be observed as deviations in both surface and bulk-sensitive fiducials, while changes to the interfacial structure would result in changes primarily to the surface-sensitive fiducial. While the absolute value of any extrinsic errors is system dependent (*e.g.* due to sample stability), the typical repeatability of fiducial measurements is ~1–2%, We typically use the observed repeatability of fiducials as a minimum error that is enforced upon the data by adding it in quadrature with the derived statistical errors derived from counting statistics.

3.5. Measurements of high-resolution specular reflectivity

Another critical test for the applicability of CCDs to measure high-resolution reflectivity profiles is the question of whether the detector has sufficient dynamic range to quantitatively probe both the strong signals near a Bragg peak (typically $R \simeq 10^{-5}$) and the much lower surface reflectivity between the Bragg peaks, with $R < 10^{-10}$. With ~90 electrons per incident photon, and a well depth of 64000 electrons, only ~700 X-ray photons can be detected for any single pixel during an exposure. A measurement of the specular reflectivity of the orthoclase (001)–water interface (Fig. 9) provides a good test of the CCD dynamic range as we have previously measured this interface using traditional approaches (Fenter *et al.*, 2003). Here we show new data obtained with the CCD detector for the orthoclase (001) surface in contact with water, and the same surface in 0.01 M RbCl. In each case the data were measured in two separate passes, with interleaved data points for the two measurements. The absence of any oscillations in the data between alternating points demonstrates the stability of the beamline, detector system and interfacial

structure. Here, individual counting times for each data point are adjusted to maintain a relatively small statistical error throughout the data. Each complete specular reflectivity profile for orthoclase (in water and 0.01 M RbCl solution) was obtained in ~1 h at the BESSRC/XOR 12-BM bending-magnet beamline. In both cases a well defined surface reflectivity is observed over the whole range of momentum transfers, with a dynamic range of ~10^4. We note that this dynamic range was obtained only with changes of counting time (ranging from ~4 to 160 s), and without any beam attenuators to reduce the scattering beam intensity near the Bragg peak. (The beam size was reduced for L < 1.2 to avoid spill-off, with the vertical beam size ranging from 0.05 mm to 0.2 mm.) Repeated fiducial measurements at selected L-values during data acquisition are a measure of extrinsic errors (due to sample evolution and detector issues). Fifteen measurements revealed statistical uncertainties of 7% and 2% at L = 1.51 and 1.9, respectively, as compared with the standard deviation of observed reflectivities, 9% and 1.8%, respectively, reinforcing the observations in Fig. 8 that the ultimate errors in these measurements are statistical in nature and that the procedures we have developed give an appropriate measure of the errors.

The ultimate test for the usefulness of such reflectivity data is the ability to obtain quantitative information concerning the interfacial structure. Full comparison of these data to structure factor calculations have been performed (solid lines, Fig. 9), confirming the geometric structure reported previously (Fenter *et al.*, 2003) for the orthoclase (001)–water interface. Measurements of orthoclase in contact with 0.01 M RbCl show significant differences with respect to that found in water, suggesting a change in interfacial structure under these conditions. Structural models for the orthoclase surface in 0.01 M RbCl show differences only in a narrow range of heights above the surface with respect to the structure in water, consistent with the adsorption of Rb$^+$ ions to the
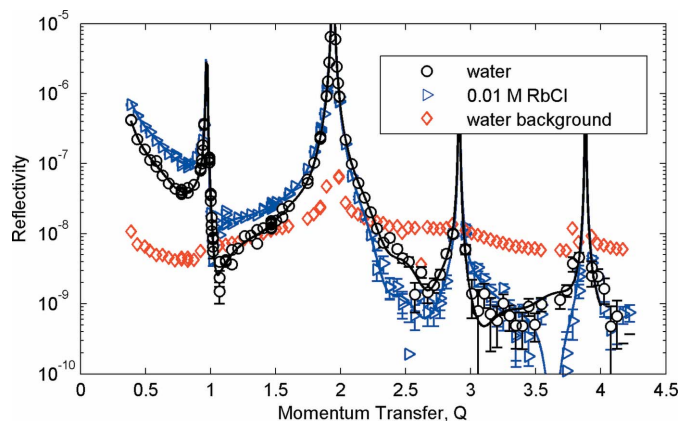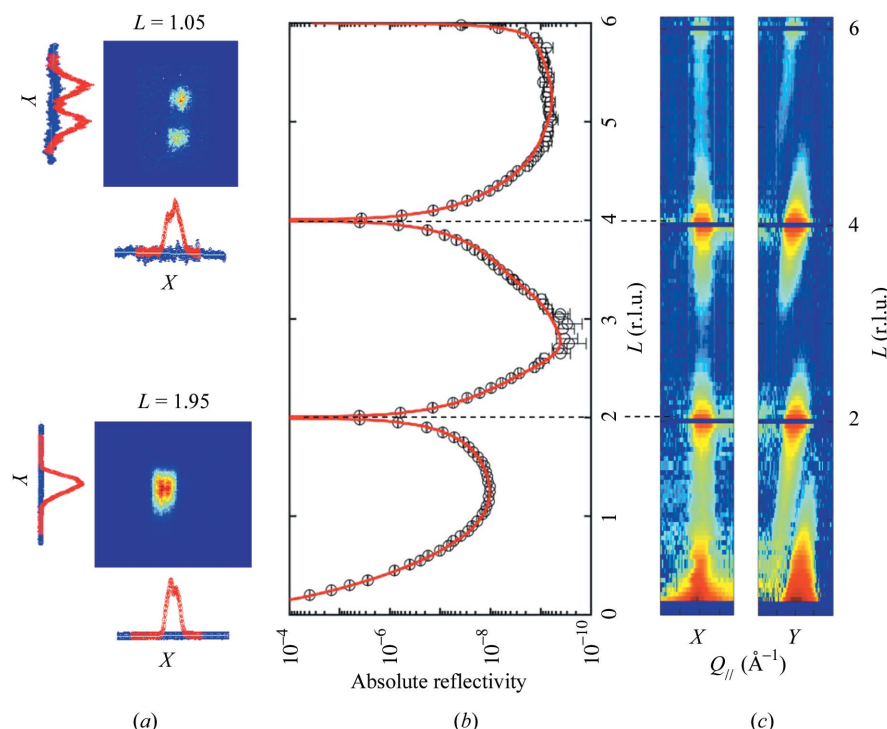

Figure 9
The specular reflectivity of the orthoclase (001)–water interface as a function of momentum transfer (in units of Å^{-1}), measured in contact with deionized water (circles) and with a 0.01 M solution of RbCl (triangles). Note that the differences in reflectivity data are well resolved for the two solution conditions. The solid lines are fits to the data. Also shown (diamonds) is the background level at each Q, scaled to indicate the signal-to-background level for each CCD image for the orthoclase in contact with water.

orthoclase surface. These results will be reported elsewhere (Fenter, 2006).

The lower limit of measurable reflectivity will be determined by two factors: the background signal level and the detector dark count rate. The background signal is shown in Fig. 9 as a function of momentum transfer (for the orthoclase–water interface) scaled to account for the fraction of the detector area within the signal box that is exposed by the reflected beam. As can be seen from these data, the statistical errors are significant when the signal becomes substantially smaller than the background level, as would be expected and as reported previously (Fenter, 2002). The lower limit of measurable reflectivity due to dark counts is determined by the product of the interfacial reflectivity and the incident beam flux. Since these measurements were performed on a bending-magnet beamline with an incident beam flux of $\sim 3 \times 10^9$ photons s^{-1}, the minimum measured reflectivity ($R \simeq 10^{-9}$) corresponds to a signal of only ~ 3 photons s^{-1} with maximum integration times of ~ 160 s, and a background signal from diffuse X-ray scattering that is about tenfold larger than the signal. This can be compared with the measured average background (dark) count rate of the CCD detector of 0.25 e$^-$ pixel^{-1} s^{-1} (at an operating temperature of 233 K). This corresponds to an X-ray photon dark count rate of $0.25 \times 1200/90 = 3$ equivalent X-ray photons per second when integrated over the beam size at the detector (~ 1200 pixels) with ~ 90 electrons produced by each X-ray photon. The combination of background signal and dark count rate provides an effective lower limit for measurable reflectivity for a given system. Similarly, a maximum count rate at the detector can also be estimated with these parameters. With the CCD pixel well depth of 64000 electrons, or ~ 700 X-ray photons at 19.5 keV, and a beam spot with ~ 1200 pixels, and a fast shutter with ~ 0.01 s time resolution, we can anticipate that the maximum X-ray flux that can be measured with this system is $\sim 10^8$ photons s^{-1}. Use of calibrated beam attenuators can arbitrarily extend this dynamic range, and consequently the same CCD detector can be used to probe both bulk and surface Bragg reflections.

We also show data for the α-Al$_2$O$_3$ (012)–water interface (Fig. 10), measured at the BESSRC/XOR 11-ID-D wiggler beamline. These data were measured with an incident photon energy of 11.8 keV, an incident beam size of 0.2 mm × 0.8 mm and a photon flux of $\sim 6 \times 10^{10}$ photons s^{-1}. The data show a clear CTR shape with a dynamic range approaching $\sim 10^6$ when plotted

in a traditional manner (Fig. 10b). Quantitative analysis of these data reveal geometrical structures that are reasonable with minimal surface roughness and small surface relaxations, and have been described in detail elsewhere (Catalano et al., 2006). As with the orthoclase data (Fig. 9), these data were obtained without the use of any beam attenuators (thereby avoiding a potential source of systematic errors), and detector saturation was avoided simply by appropriately choosing the detector integration time from 0.5 s to 200 s to obtain sufficient statistics while avoiding saturation. These data show a minimum reflectivity at $\sim 5 \times 10^{-10}$ near $L = 3$, which corresponds to a count rate at the CCD of 30 X-ray photons s^{-1} at 11-ID-D. This is significantly larger than the dark count rate of the CCD (~ 6 equivalent X-ray photons s^{-1} at this photon energy) illustrating that the results are not limited by the CCD dark count rate. These data were obtained in 2.5 h with a variation of repeated fiducial measurements at $L = 3.9$ of 1.8%, which can be compared with the derived statistical uncertainty of 2.1% suggesting that the sample and detector were stable over the course of the measurements. A more judicious choice of integration times, as well as the increased flux afforded by an undulator source at the Advanced Photon Source (with useful flux that is 10- to 100-fold larger than the 11-ID-D wiggler source), would lead to the ability to obtain complete structural measurements with <1 Å resolution and

Figure 10
Specular reflectivity of the α-Al$_2$O$_3$ (012)–water interface. (a) Individual CCD images at $L = 1.05$ and 1.95, showing a splitting at $L = 1.05$ due to a surface that is miscut by 0.14° with respect to the crystallographic (012) plane. Also shown are one-dimensional integrations of the individual spectra along X and Y, as described in Fig. 4. (b) Specular reflectivity of the surface in water measured at the 11-ID-D beamline (red triangles). The solid line is a best-fit calculation. (c) The same data as in (b) but shown as a projection of the full three-dimensional CCD data set onto the Q_z–$Q_{//}$ plane (note that the aspect ratio is distorted with a $Q_{//}$ range that is greatly exaggerated for clarity). Two projections are shown along the X and Y axes of the CCD images. Note that the splitting of the rod along the Y direction is not seen in the X projection.

with similar statistical quality in <15 min. Even under these circumstances the overhead time associated with communication between computers, data transfer rates and diffractometer motion would only add a minor contribution to the measurement time.

Another benefit of the use of area detectors is the ability to visualize complex structures in reciprocal space. An example of this can be seen in two-dimensional projections of the three-dimensional reflectivity data, shown as a function of $Q_z = L(2\pi/d_{001})$ and $Q_{//}$, with $Q_{//}$ along either the X or Y axes of the individual CCD images (Fig. 10c). The data in the X projection show a specular rod that appears continuously at all L values but with the intensity weakest near $L = 3$, consistent with the traditional plotting of the data where the statistical error becomes significant. In contrast, the Y projection shows that the CTR is tilted due to the miscut of the physical surface with respect to the crystallographic plane of $0.14°$. This is seen in individual CCD images as a splitting of the specular rod near the anti-Bragg condition ($L \simeq 1.05$) but a single peak near the Bragg peak ($L = 1.95$), as seen in Fig. 10(a). Some care is required to probe the structure of miscut surfaces, since the two rods will typically intersect the Ewald sphere at different Q_z values (and therefore with different inherent reflectivities). Use of a CCD to probe miscut surfaces therefore requires either independent measurements of the two rods or pre-aligning the surface so that the miscut is aligned along the ν direction. In this way the two sections of the rod are always measured under the same Q_z scattering condition.

3.6. Dependence of CCD efficiency *versus* X-ray photon energy

The CCD sensitivity varies with X-ray photon energy. This is important when using the CCD detector to probe interfaces using resonant anomalous X-ray reflectivity, in which the reflectivity is probed as a function of photon energy at fixed Q (Park *et al.*, 2005). We probed the CCD sensitivity to photon energy in two separate ways. First, we measured the relative sensitivity of the CCD detector as a function of energy for a single sample, by integrating the same reflection of the orthoclase (001)–water interface at $L = 1.9$ at various energies, with corrections for the beam monitor sensitivity using the nominal energy-dependent absorption of the X-ray beam in the ion chamber. These data ('relative sensitivity' in Fig. 11) show an approximately linear variation of CCD sensitivity with photon energy. We also made direct comparison of the CCD signal with that measured by a scintillator detector for various photon energies and various samples ('absolute sensitivity' in Fig. 11) between ~7 keV and ~20 keV. These results demonstrate that the variation of CCD sensitivity with photon energy is linear. Error in individual data points is associated with the fact that the absolute measurements were carried out with different samples and photon energies on two different beamlines (BESSRC/XOR 11-ID-D and 12-BM), while the relative measurements were made on a single sample but were corrected only for nominal monitor sensitivity. This linear variation is expected since the optical phosphorescence
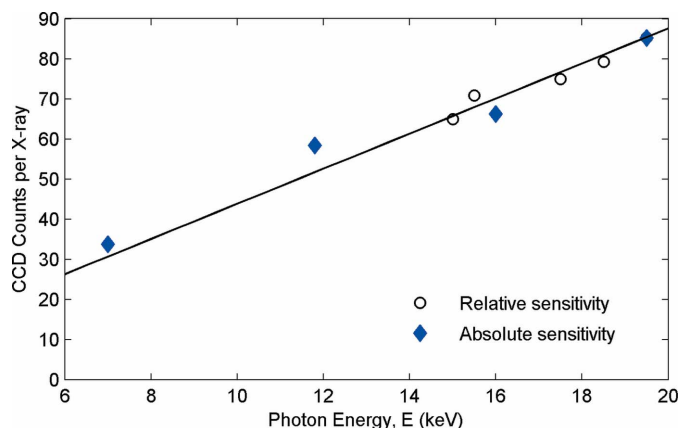
Figure 11
Sensitivity of the CCD detector as a function of photon energy, plotted as the number of CCD counts per detected X-ray photon. Data labeled 'absolute sensitivity' (closed symbols) indicate a direct comparison of intensities measured with both scintillator and CCD detectors obtained under the same scattering condition and on the same sample. Data labeled 'relative sensitivity' (open symbols) indicate the fraction changes in sensitivity of the CCD with respect to a measurement at 19.5 keV, after correcting for the nominal energy-dependent sensitivity of the ion chamber used as a monitor. The solid line corresponds to the calibration curve with the number of CCD counts per X-ray photon expressed as $4.38 \times E$ (keV).

of the CCD phosphor should be proportional to the absorbed energy which is in turn proportional to the photon energy. This photon calibration curve is needed to convert electron counts in the CCD images to the number of detected X-rays (and ultimately to absolute structure factors) obtained with different X-ray photon energies. These data show that the detector sensitivity is a slowly varying function of photon energy and that a correction for this can be included in a straightforward manner during data analysis to obtain appropriate error propagation.

3.7. Use of CCDs for measurements of crystal truncation rods

The present results illustrate the use of CCD area detectors for the measurement of high-resolution X-ray specular reflectivity. Application of this approach to measuring non-specular crystal truncation rods should follow in a straightforward manner from the procedures presented here for the specific case of specular reflectivity. In general, the approach described here will be best suited to probe CTR structures at sufficiently large exit angles so that the intersection of the CTR with the CCD detector results in a distinct spot on the CCD, whose intensity is indicative of the structure factor at a specific Q_z. At sufficiently low Q_z the tangential intersection of the Ewald sphere with the CTR will result in a streak instead of a distinct spot. Under these conditions it may be necessary to integrate a section of the rod by rocking the sample, as described previously (Hong *et al.*, 2002).

Since the size of the scattered beam will not typically be the same as the incident beam, some care will be needed to ensure that scattered beams with elongated cross sections (*e.g.* due to the incident-beam footprint on the sample surface) are fully

accepted by the detector slits. In this respect the use of the CCD detector should be beneficial since it can work with open slits and integrate all of the elastically scattered radiation from areas of the sample illuminated by the incident beam without any reduction of signal to background. This, in effect, can eliminate the need for active area corrections that derive from the overlap of the areas simultaneously visible to the incident beam and the detectors, and consequently make the conversion of intensity to structure factor more precise. The general relationship between intensities and structure factor using this open-slit geometry for an arbitrary non-specular reflection geometry without rocking scans has been described previously (Specht & Walker, 1993).

4. Summary

These results demonstrate the application of CCD area detectors for measuring high-resolution X-ray reflectivity data. The use of CCD detectors leads to substantial reduction in the necessary measurement time (typically by factors of ~ 30 to 50). Because of the increased data acquisition rate in this geometry, the CCD detector may substantially reduce systematic errors due to changes in the surface structure or morphology during measurement that may result from inherent kinetic changes, instabilities in the sample environment or from X-ray-induced perturbation of the sample (*i.e.* beam damage). This more rapid data acquisition opens up the possibility of directly observing molecular-scale processes at mineral–water interfaces with <1 Å resolution and in real time with ~ 15 min time resolution with complete structural analysis performed at each time point. This would be appropriate for relatively slow processes such as mineral dissolution, where individual layers are removed at rates ranging from minutes to hours, as controlled by the temperature and pH. The CCD detector also offers an increased angular resolution in probing the shape of the reflected rod with respect to using a scintillator detector in the traditional scattering geometry. Associated with this is an increase in signal-to-background ratio which further reduces the time needed for data acquisition.

References

Als-Nielsen, J. & McMorrow, D. (2001). *Elements of Modern X-ray Physics.* New York: John Wiley.
Beno, M. A., Engbretson, M., Jennings, G., Knapp, G. S., Linton, J., Kurtz, C., Rutt, U. & Montano, P. A. (2001). *Nucl. Instrum. Methods*, A**467**, 699–702.
Beno, M. A., Jennings, G., Engbretson, M., Knapp, G. S., Kurtz, C., Zabransky, B., Linton, J., Seifert, S., Wiley, C. & Montano, P. A. (2001). *Nucl. Instrum. Methods*, A**467**, 690–693.
Bevington, P. R. (1969) *Data Reduction and Error Analysis for the Physical Sciences.* New York: McGraw-Hill.
Bloch, J. M. (1985). *J. Appl. Cryst.* **18**, 33–36.
Busing, W. R. & Levy, H. A. (1967). *Acta Cryst.* **22**, 457–464.
Catalano, J. G., Park, C., Zhang, Z. & Fenter, P. (2006). *Langmuir*, **22**, 4668–4673.
Feidenhans'l, R. (1989). *Surf. Sci. Rep.* **10**, 105–188.
Fenter, P. (2006). In preparation.
Fenter, P., Cheng, L., Park, C., Zhang, Z. & Sturchio, N. C. (2003). *Geochim. Cosmochim. Acta*, **67**, 4267–4275.
Fenter, P., McBride, M. T., Srajer, G., Sturchio, N. C. & Bosbach, D. (2001). *J. Phys. Chem. B*, **105**, 8112–8119.
Fenter, P. & Zhang, Z. (2005). *Phys. Rev. B*, **72**, 081401R(1–4).
Fenter, P. A. (2002). *Rev. Mineral. Geochem.* **49**, 149–220.
Hong, H. W., Wu, Z., Chiang, T. C., Zschack, P. & Chen, H. D. (2002). *Rev. Sci. Instrum.* **73**, 1720–1723.
Lyman, P. F., Shneerson, V. L., Fung, R., Harder, R. J., Lu, E. D., Parihar, S. S. & Saldin, D. K. (2005). *Phys. Rev. B*, **71**, 081402(R).
Naudon, A. & Thiaudiere, D. (1997). *J. Appl. Cryst.* **30**, 822–827.
Park, C., Fenter, P., Sturchio, N. C. & Regalbuto, J. R. (2005). *Phys. Rev. Lett.* **94**, 076104.
Rivers, M. L. (2005). Personal communcation. [For more information, see http://cars9.uchicago.edu/software/epics/.]
Robinson, I. K. (1986). *Phys. Rev. B*, **33**, 3830–3836.
Robinson, I. K. (1988). *Aust. J. Phys.* **41**, 359–367.
Robinson, I. K. (1991). *Surface Crystallography.* In *Handbook on Synchrotron Radiation*, Vol. 3, edited by G. S. Brown and D. E. Moncton, pp. 223–266. Amsterdam: North Holland.
Robinson, I. K., Eng, P. & Schuster, R. (1994). *Acta Phys. Pol. A*, **86**, 513–520.
Robinson, I. K., Tabuchi, M., Hisadome, S., Oga, R. & Takeda, Y. (2005). *J. Appl. Cryst.* **38**, 299–305.
Robinson, I. K. & Tweet, D. J. (1992). *Rep. Prog. Phys.* **55**, 599–651.
Schlepütz, C. M., Herger, R., Willmott, P. R., Patterson, B. D., Bunk, O., Brönnimann, C., Henrich, B., Hülsen, G. & Eikenberry, E. F. (2005). *Acta Cryst.* A**61**, 418–425.
Specht, E. D. & Walker, F. J. (1993). *J. Appl. Cryst.* **26**, 166–171.
Vlieg, E., van der Veen, J. F., Macdonald, J. E. & Miller, M. (1987). *J. Appl. Cryst.* **20**, 330–337.
You, H. (1999). *J. Appl. Cryst.* **32**, 614–623.